Engineering Fracture Mechanics 281 (2023) 109146

Contents lists available at ScienceDirect

Engineering Fracture Mechanics

journal homepage: www.elsevier.com/locate/engfracmech

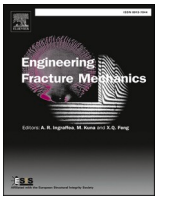

Microstructure-based cleavage parameters in bainitic, martensitic, and ferritic steels

Quanxin Jiang [a,*], Virgínia M. Bertolo [a], Sakari Pallaspuro [b], Vera Popovich [a], Jilt Sietsma [a], Carey L. Walters [c,d]

[a] Materials Science and Engineering, Delft University of Technology, Delft, The Netherlands
[b] Materials and Mechanical Engineering, Centre for Advanced Steels Research, University of Oulu, Oulu, Finland
[c] Maritime and Transport Technology, Delft University of Technology, Delft, The Netherlands
[d] Structural Dynamics, TNO, Delft, The Netherlands

ARTICLE INFO

Keywords:
Cleavage
Statistical modelling
Fracture toughness
Multi-barrier modelling
Local approach to fracture

ABSTRACT

Multi-barrier cleavage models consider cleavage fracture which is characterized by a series of microscale events. One of the challenges for multi-barrier cleavage models is the strong variations of cleavage parameters across different types of steels. The source and magnitude of the variations have not been studied systematically. In the current paper, cleavage parameters corresponding to fracture initiation at a hard particle and crack propagation overcoming grain boundaries are determined for three bainitic steels, a martensitic steel, and a ferritic steel, using a recently proposed model. It is found that the particle fracture parameter depends on particle morphology and composition, while the grain boundary cleavage parameter depends on the hierarchical grain structure. The determined values of cleavage parameters present a high degree of consistency among the five different steels, which allows the further application on microstructure design to control macroscopic toughness.

1. Introduction

Cleavage fracture shows strong sensitivity to material characteristics at the microstructural level, such as grain size [1], carbide size [2], hard inclusions [3], M−A (martensite-austenite) phases [4], precipitates [5], etc. The local approach to cleavage fracture is a class of physics-based statistical models that account for the probability of failure based on the local stress (and sometimes strain) field [6]. The Weibull formulation based on the weakest-link mechanism was first proposed by the Beremin group [7], Wallin et al. [8], and Lin et al. [9]. Many attempts [10–14] were made to represent the statistical distribution of cleavage toughness based on the Weibull formulation. More recently, studies presented predictions of the toughness of steels from their microstructural information [15–17], which have shown that the models using microstructural information could accurately predict cleavage fracture in steels without employing the macroscopic cleavage parameters.

Among these models, effective surface energy γ_{eff} was proposed based on Griffith's criterion [18,19] for simulating elastoplastic materials [20]. γ_{eff} is dependent on the local plastic behaviour of the matrix, and thus varies among different types of microstructures.

Abbreviations: M−A, Martensite-Austenite; PAG, Prior Austenite Grain; K-S, Kurdjumov-Sachs; EBSD, Electron Backscatter Diffraction; FEA, Finite Element Analysis; CTOD, Crack Tip Opening Displacement; SENB, Single-Edge Notched Beam.

* Corresponding author at: Mekelweg 2, 2628 CD Delft, The Netherlands.
E-mail address: q.jiang-1@tudelft.nl (Q. Jiang).

https://doi.org/10.1016/j.engfracmech.2023.109146
Received 10 October 2022; Received in revised form 5 February 2023; Accepted 19 February 2023
Available online 22 February 2023

Nomenclature

a	Initial crack length of SENB specimen
B	Thickness of SENB specimen
f_α	Stress concentration factor of inclusion
K_{Ia}^{mm}	Crack arrest parameter of grain boundary
K_{Ia}^{pm}	Crack arrest parameter of particle matrix interface
K	Hardening parameter of matrix
n_L	Hardening exponent of matrix
N	Number of potential cracking nuclei per unit volume
N_{cr}	New microcrack per unit volume during a load increment
$P(D)$	Distribution function of the grain size D
$P(d)$	Distribution function of the particle size d
P_f	Fracture probability
S	Span of SENB specimen in the three-point bending test
V_0	Elementary volume
W	Width of SENB specimen
γ_{pm}	Surface energy when crack propagates into the matrix
γ_{mm}	Surface energy when crack propagates across a grain boundary
$\Delta\sigma_H^C$	Scatter of the inclusion fracture strength
ε_p	Von Mises equivalent plastic strain
$\varepsilon_{p,t}$	Threshold value of plastic strain
$\sigma_{1,m}$	Matrix first principal stress
$\sigma_{eq,m}$	Matrix Von-Mises equivalent stress
σ_{H}	Representative inclusion stress
σ_H^c	Critical stress for hard inclusion cracking
σ_y	Yield strength

There are two effective surface energy terms that are used: γ_{pm}, which represents the resistance of crack propagation from a brittle particle into the matrix; and γ_{mm}, which represents the resistance of crack propagation across a grain boundary [20]. The values of γ_{pm} and γ_{mm} have been reported from experimental estimations. Curry et al. [21] fitted γ_{pm} as 14 J/m^2 in a spheroidized ferrite/cementite steel. Bowen et al. [22] calculated γ_{pm} from the size of the carbide and the local fracture stress, and the resulting values vary in a range of 7–9 J/ m^2. Alexander et al. [23] calculated γ_{pm} to be 5–10 J/m^2 for pearlite eutectoid steel with a similar method. Linaza et al. estimated γ_{pm} for Ti bearing steels and Mn/B steels, and the resulting values vary in a range of 10–30 J/m^2 [24]. The value of γ_{mm} is more rarely determined and shows a wide variation in the values. Linaza calculated γ_{mm} to be 50–200 J/m^2 in [25]. A rapid increase of the estimated γ_{mm} from 50 J/m^2 at 173 K to 500 J/ m^2 at 223 K was reported by San Martin and Rodriguez-Ibabe [26]. Kawata et al. measured a range 25–100 J/m^2 of γ_{mm} for Ni-steels, depending on the temperature of measurement [27]. Li et al. measured the ratio $\gamma_{\mathrm{mm}}/\gamma_{\mathrm{pm}}$ [28], and calculated γ_{mm} indirectly from γ_{pm}, which resulted in a range of 50–250 J/m^2.

A model based on multi-barrier theory was developed in [10,15] for the prediction of cleavage fracture based on a statistical distribution of microstructural parameters and was recently improved through the incorporation of hard-particle deactivation in [29] for bainitic steels by the authors of this paper. The model is focused on inclusion cracking and the propagation of a microcrack through the first grain boundary. Cleavage parameters K_{Ia}^{mm} (crack arrest toughness of the grain boundary), and σ_H^C (fracture stress of hard inclusion) are fitted from fracture experiments. Previous analysis of a commercially available 80 mm thick S690 QT steel [29,30] has been used to illustrate the modelling method and reveals the critically weak microstructural links in cleavage fracture. In the present paper, cleavage parameters of this model are determined for a commercially available 80 mm thick S690 QT steel (S690-A1) [29,30], a variation of this commercial steel without Nb content (S690-A2), a commercial 100 mm thick S690 QT steel from a different provider (S690-B), a low-carbon martensitic steel [31], and a ferrite-cementite steel [32]. The variation of cleavage parameters is estimated and discussed considering thickness positions in S690 steel plate, chemical compositions, and process profile for the same 690 strength

Table 1
Chemical composition of steels in wt% (- stands for not detected).

Materials	C	Si	Mn	P	S	N	Al	Mo	Others*
S690-A1 [30]	0.17	0.29	1.29	0.009	< 0.002	0.005	0.067	0.304	Ni, Cr, Nb
S690-A2	0.17	0.25	1.01	0.012	<0.002	0.003	0.03	0.48	Ni, Cr, Ti
S690-B	0.097	0.07	0.94	0.006	0.004	<0.002	0.06	0.43	Ni, Cr, V, Cu
Martensitic [31]	0.124	0.20	1.08	0.007	0.002	0.005	0.03	0.155	Cr, Ti
Ferritic [32]	0.05	0.05	0.48	<0.002	0.0003	0.0014	0.01	–	–

*wt% is regarded as commercial confidential information and can be provided upon request.

class, matrix types (bainite, martensite, ferrite), and hard particle types.

2. Materials and characterization

Three types of S690 quenched-tempered bainitic-martensitic steels (S690-A1, S690-A2, and S690-B), one martensitic steel, and one ferritic steel are studied in this paper. Table 1 shows the chemical composition of the five steels. The material S690-A1 is taken from a commercially available 80 mm thick steel plate. S690-A2 is a custom-made steel with the same nominal characteristics as S690-A1 but of a different chemical composition. Samples of S690-B are taken from another type of commercially available 100 mm thick steel plate. Materials of S690 steels are extracted from the top quarter section and the middle section of the plate. S690-A2 and S690-B are characterized and tested in this paper while S690-A1 has been characterized and tested in [30]. The martensitic steel and the ferritic steel have been characterized and tested by [31] and [32], respectively. All the steel plates were formed by hot-rolling.

2.1. Phases

Representative microstructures of the steels are shown in Fig. 1 (micrographs of S690-A2 represent microstructures of the S690 steels). For the three types of S690 steel, both the top and middle sections of the plate have microstructures of 70–80% tempered bainite and 20–30% tempered martensite. The mid-thickness appears to have a higher fraction of tempered martensite and more pronounced segregation banding [30]. The microstructure of the martensitic steel is 90% auto-tempered lath-martensite and 10% untempered lath-martensite [31]. The ferritic steel has a ferrite–pearlite microstructure with coarsened cementite particles [32].

2.2. Grain sizes

For lath microstructure such as bainite and martensite, “grains” show hierarchy structures, that ideally, individual Prior Austenite Grains (PAGs) are divided into four distinguishable packets that have the same Kurdjumov-Sachs (K-S) variant, and each packet is composed of three blocks of different Bain variants [33]. PAG size is used as the representative microstructural factor in the current analysis with the assumption that PAG size is linearly correlated to K-S packet size and to the possible cleavage facet size. For the bainitic steels and the martensitic steel, microstructural unit defined on the basis of the misorientation angle results in a large portion of ultra-small areas that do not act as cleavage facets. More discussions of the grain definitions are presented in Section 5.

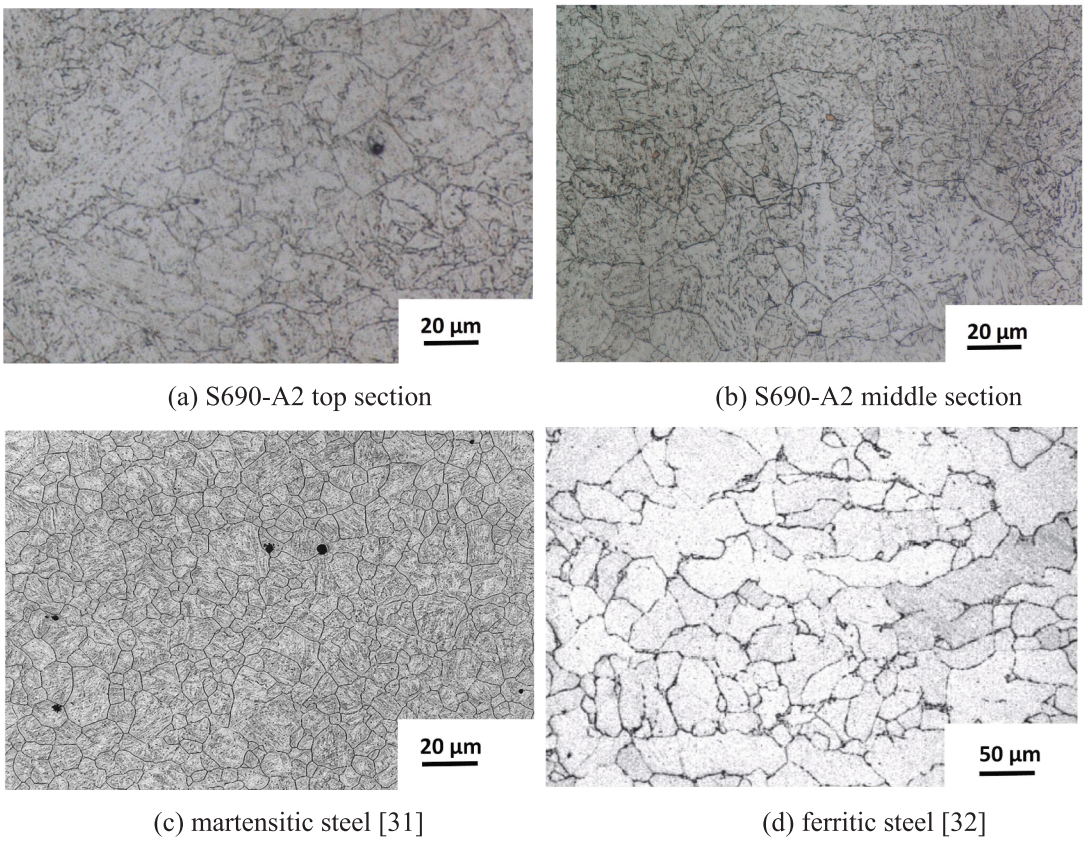

(a) S690-A2 top section (b) S690-A2 middle section

(c) martensitic steel [31] (d) ferritic steel [32]

Fig. 1. Micrographs of bainitic (S690), martensitic, and ferritic steels.

For the three types of S690 steels, PAG, later referred as "grains", are reconstructed from Electron Backscatter Diffraction (EBSD) data in the top section and the middle section of the steel plate. EBSD data was acquired on a JEOL scanning electron microscope equipped with a Field Emission Gun (FEG-SEM) using 25 kV accelerating voltage, working distance of 25 mm, tilt angle of 70°, and step size 0.2 μm; obtained by means of HKL Channel 5 software and post-processed with EDAX-TSL-OIM AnalysisTM software. The statistical distribution of grain size has been measured based on the major axis of PAGs, as the average aspect ratio (minor axis/major axis) is found to be 0.5 for the S690 steels. To quantify the grain size (D) in cleavage modelling, least-square fitting is performed on the grain size data to get the function $P(D)$ representing the probability of grains larger than D. $P(D)$ is a combined function of lognormal distribution and power-law distribution, in order to accurately reflect the tails:

$$P(D) = \min\left\{1 - f(D,\mu,S), \frac{\alpha}{D^{\beta}}\right\} \tag{1}$$

with $f(D,\mu,S)$ represents equation $1/2 + 1/2\mathrm{erf}(\frac{\ln D-\mu}{\sqrt{2}S})$, where α and β are fitting parameters, μ is the mean and S is the standard deviation.

Fig. 2 shows the distribution function of each type of steel and the examples of the data measured in S690-A2 to indicate the goodness of fit. For all the S690 steels, the top sections have smaller grains and the middle section have slightly larger grains. For the martensitic steel, the PAG size was measured as equivalent circle diameter from etched micrographs, and eq. (1) is fitted to data published in [31]. For ferritic steel, there is no hierarchy grain structures and the grain boundaries are defined as boundaries where misorientation is larger than 5° measured by EBSD [32]. The ferrite grain size is defined as the equivalent circle diameter and eq. (1) is fitted to data published in [32]. Fig. 2 shows that of all the five steels the martensitic steel has the finest prior austenite grains, and the ferritic steel has the coarsest grains.

2.3. Hard particles

Quantification of size of inclusions in S690 steels was performed by Keyence optical microscope. For S690-A1 and S690-A2, circular and square inclusions were observed in both top and middle sections. The size of circular inclusions is measured as equivalent diameter, while the square inclusions are represented by the longer axis. Fig. 3 shows the statistical distribution of particle size fitted by eq. (1) for the five steels. Volume density of inclusions is calculated from 2D measurement according to Schwartz-Saltykov method [34], and is listed in Table 2 for the S690 steels. Less circular and more square inclusions are present in S690-A2 steel than in S690-A1 steel. For square inclusions, the density in the middle section is higher, and the square inclusions tend to be larger compared to circular inclusions. S690-B steel contains smaller circular inclusions than the S690-A1 and S690-A2, and does not show square inclusions.

The inclusions in the martensitic steel can be divided into four groups based on the main element: aluminium, calcium, manganese, and titanium. Within these groups, there are nitrides, oxides, sulphides, and mixed types. The total number of mapped inclusions is 3651 in a 46 mm^2 area and 19.2% of the total inclusions are Ti-rich inclusions in square shape [31]. The circular shape inclusions and the square shape inclusions do not show difference in their size distributions. Compared with S690-A1 and S690-A2, the material has a higher frequency of smaller inclusions ($d < 2$ μm), which is similar to S690-B.

The hard particles that initiate cleavage in the ferritic steel are reported as cementite in [32]. The particle size was identified as a minor axis of an approximated ellipse because the crack was observed to generally occur in this direction [32]. The volume fraction of cementite was calculated from the carbon concentration, assuming cementite to contain 6.67% (wt) carbon. The shape of the particles is assumed as an oblate spheroid with the aspect ratio of 3.45 as reported in [32]. While S690 steels and martensitic steels have inclusions larger than 1 μm, cementite in the ferritic steel has sub-micro size.

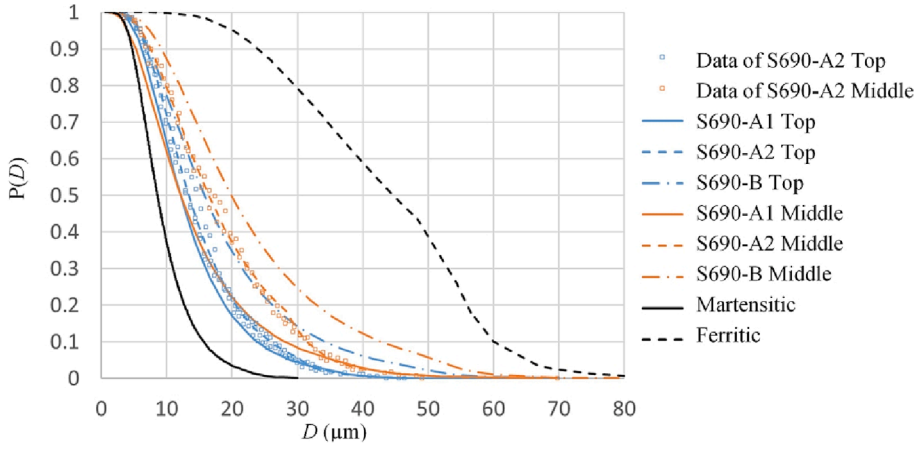

Fig. 2. Statistical distributions of the grain size obtained by fitting eq. (1) to experimental data, with examples of the data of S690-A2.

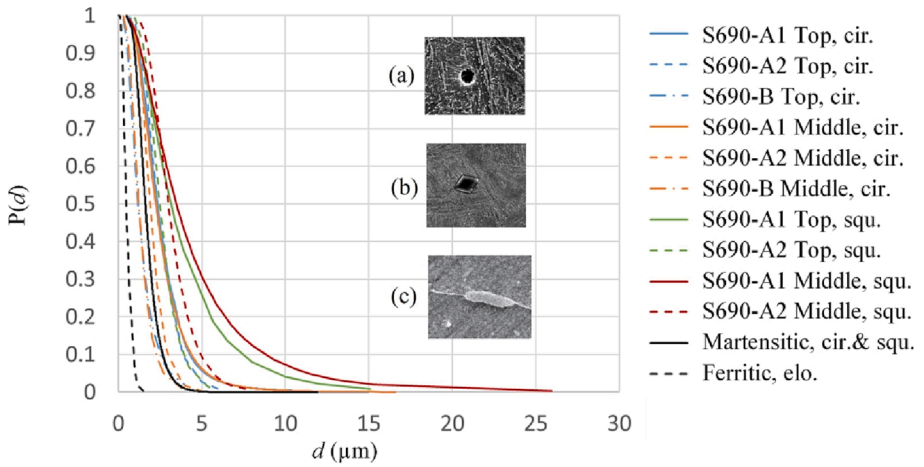

Fig. 3. Statistical distributions of the particle size obtained by fitting eq. (1) to experimental data, with figures showing the examples of (a) circular (cir.) inclusions, (b) square (squ.) inclusions, and (c) elongated (elo.) cementite.

Table 2
Inclusion number per 0.001 mm^3 (- stands for not detected).

Inclusion types	S690-A1		S690-A2		S690-B	
	Top	Middle	Top	Middle	Top	Middle
circular inclusion	43.1	38.3	2.5	5.8	5.0	7.8
square inclusion	1.0	13.1	9.6	11.2	–	–

2.4. Tensile properties

The stress–strain relationship of the steels is characterized by Ludwik's law, which is defined with the flow stress (σ) and the effective plastic strain (ε_p) as:

$$\sigma = \sigma_y + K\varepsilon_p^{n_L} \tag{2}$$

where σ_y is fitted yield stress, K and n_L are hardening parameters. For the steel S690-A2 yield point elongation is observed and in the strain range of elongation $\sigma = \sigma_{y,0.2}$ with $\sigma_{y,0.2}$ the 0.2% proof stress determined from the tensile curve. The parameters of Ludwik's law are fitted from tensile tests and are used to generate material input for the Finite Element Analysis (FEA).

Tensile tests of S690 steels were carried out at the temperature corresponding to the fracture tests (-100 °C for S690-A1 and S690-A2, –130 °C for S690-B) for top and middle specimens. The tensile tests of martensitic steel were performed at room temperature [31]. Since unstable necking occurs at a relatively low strain level, Digital Image Correlation data is used to generate the true-stress, true-

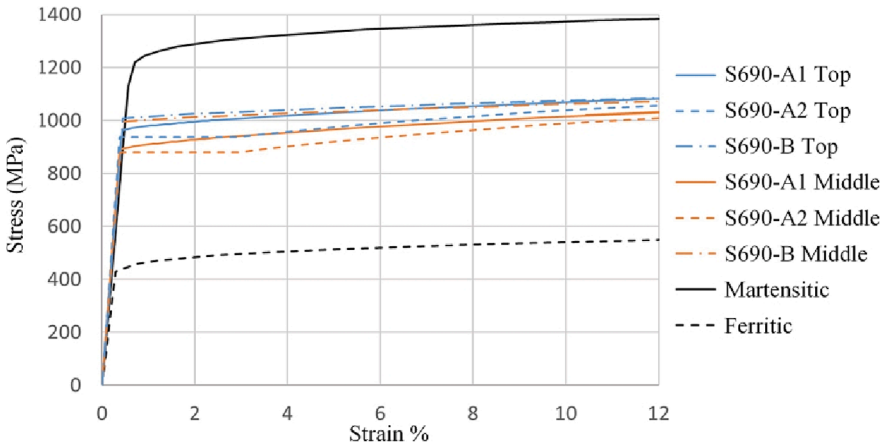

Fig. 4. True stress vs True strain curve of S690-A1 (at −100 °C), S690-A2 (at −130 °C), S690-B (at −130 °C), martensitic steel (at room temperature), and ferritic steel (at −110 °C) obtained by fitting eq. (2) to experimental data.

stain curve after the maximum force. The fracture tests were performed at −60 °C, −40 °C and −20 °C. The true stress–strain curves at lower temperatures were derived from the tensile test at room temperature according to [35]. For the ferritic steel, tensile tests were conducted at −110 °C, which is the same temperature as for the fracture tests [32]. The entire curve reported in [32] includes a tensile test until the maximum load and extrapolation after it. Eq. (2) is used to fit parameters for FEA based on the reported tensile curve. Fig. 4 shows the summary of fitting results while Table 3 summarize the yield strength and ultimate tensile strength.

3. Method of simulating cleavage fracture

This section outlines the method to model the cleavage probability of macroscale specimens, which are then used to determine the unknown cleavage parameters. Finite element analysis (FEA) of a macroscopic volume gives the result of stress/strain distribution under a certain global load level. The cleavage probability of each finite element is calculated as a function of stress level and will be evaluated based on the volume of the finite element. The total failure probability of the specimen can be expressed as a function of the global load. Each combination of cleavage parameters K_{Ia}^{pm}, K_{Ia}^{mm} and σ_H^C can generate a probability distribution of CTOD of specimens. In this article, the unknown values of cleavage parameters are determined by inverse analysis based on the cumulative distribution of all admissible CTOD values.

3.1. Statistical model

The model applied in this paper is developed in [29] based on a multiple-barrier theory of the cleavage mechanism [10,15]. Cleavage fracture of steels is regarded as the result of successive occurrence of three events:

I: nucleation of a slip-induced crack at a brittle second-phase particle or inclusion;

II: propagation of the microcrack across the particle/matrix interface;

III: propagation of the grain-sized crack to neighbouring grains across the grain boundary.

Inclusions and second phase particles are associated with the fracture initiation (event I). Under plastic flow, stress in a second phase particle is raised to a level to nucleate a microcrack. If the particle is brittle and deforms elastically during cracking, a single-parameter condition can be motivated for crack nucleation, where a critical-strain-based model can be uniquely transformed into a critical-stress-based model [6]. The stress level needed for inclusion cleavage is characterized by particle strength σ_H^C. It is assumed that the value of inclusion strength is uniformly distributed in the range $[\sigma_H^C, \sigma_H^C + \Delta\sigma_H^C]$. For a volume that contains N inclusions, the number of cracked inclusions (N_{cr}) is in proportion to the stress σ_H at the inclusion, and can be calculated f or $\sigma_H > \sigma_H^C$ as:

$$N_{cr} = \min\{N \times (\sigma_H - \sigma_H^C)/\Delta\sigma_H^C, N\} \tag{3}$$

where the stress σ_H at the inclusion is calculated from the first principal stress of the matrix $\sigma_{1,m}$ and the equivalent von Mises stress of the matrix $\sigma_{eq,m}$, by

$$\sigma_H = \sigma_{1,m} + f_\alpha \sigma_{eq,m} \tag{4}$$

where the factor f_α is determined using the analytical solution in [36] based on the inclusion geometry. In eq. (4), $\sigma_{eq,m}$ increases with plastic strain for a strain-hardening material, and f_α is always positive for an elastic inclusion. As a result, the calculated inclusion stress σ_H increases with plastic strain, and given eq. (3), the number of cracked particles also increases with plastic strain [36]. It agrees with the finding in [37,38,39], based on observations of initiation sites triggering cleavage fracture in ferrite-pearlite steels.

Phase boundaries and grain boundaries in ferritic steels offer important resistance to the propagation of cleavage cracks. When the cracks nucleated in particles encounter the much tougher surrounding matrix material, the crack may deflect into the interface (event II) instead of penetrating the surrounding matrix [40]. When an advancing crack front meets a grain boundary, its propagation path can be deflected due to the large misorientation of cleavage planes (event III) [41]. A critical stress is usually used as a criterion for the crack propagation across the particle/matrix interface or across the grain boundary. In the present paper, the equivalent matrix toughness at the particle/matrix interface is characterized by the local cleavage parameter K_{Ia}^{pm}, and the equivalent toughness at the grain boundary is characterized by the local cleavage parameter K_{Ia}^{mm}. A minimum particle size (d_c) and a minimum grain size (D_c) are calculated for the first principal stress within the grain ($\sigma_{1,m}$) to propagate the micro-crack across the particle/matrix interface and grain boundary, respectively by:

$$d_c = (K_{Ia}^{pm}/\sigma_{1,m})^2 \tag{5}$$

Table 3
Yield strength and ultimate tensile strength in Fig. 4.

Material	S690-A1		S690-A2		S690-B		martensitic	ferritic
Section	top	middle	top	middle	top	middle	-	-
Yield strength (MPa)	962	882	936	880	996	975	963	512*
Tensile strength (MPa)	1063	1004	1034	972	1000	977	1252	565*

* Approximated values from plots in[32].

$$D_c = (K_{Ia}^{mm}/\sigma_{1,m})^2 \tag{6}$$

The parameters K_{Ia}^{pm} and K_{Ia}^{mm} represent the equivalent effect of the boundaries, and eq. (5) and (6) do not assume the shape of the micro-crack. The micromechanism of crack propagation in the present paper is also comparable with conventional models using surface energy in [16,17], where critical microcrack size is positively proportional to γ_{eff} and negatively proportional to the square of local fracture stress.

Fig. 5 gives a flow chart of the computational model to calculate the cleavage probability of macroscale specimens. (FEA gives the stress/strain distribution (which contains $\sigma_{1,m}$, $\sigma_{eq,m}$, and ε_p values for each finite element). The cleavage probability is calculated from a cleavage check based on the stress level, shape of the stress field, and statistical information of the microstructure. By accounting for the cleavage probability of all finite elements in the fracture process zone (areas that are plastically deforming), the total failure probability (*Pf*) of the specimen is calculated and expressed as a function of the global load. In addition to FEA stress and strain results, the required input includes f_α calculated from inclusion geometry, the distribution density function of the grain size $P(D)$, the distribution density function of the hard particle size $P(d)$, number of inclusions N per unit of volume, cleavage parameters K_{Ia}^{pm}, K_{Ia}^{mm} and σ_H^C. Other predefined parameters are threshold plastic strain $\varepsilon_{p,t}$, elementary volume V_0, and scatter of the inclusion fracture strength $\Delta\sigma_H^C$. All predefined values are summarized in Table 4.

3.2. Finite element model of fracture toughness tests

Fracture tests of all types of steels were conducted on single-edge notched beam (SENB) specimens with static loading conditions,

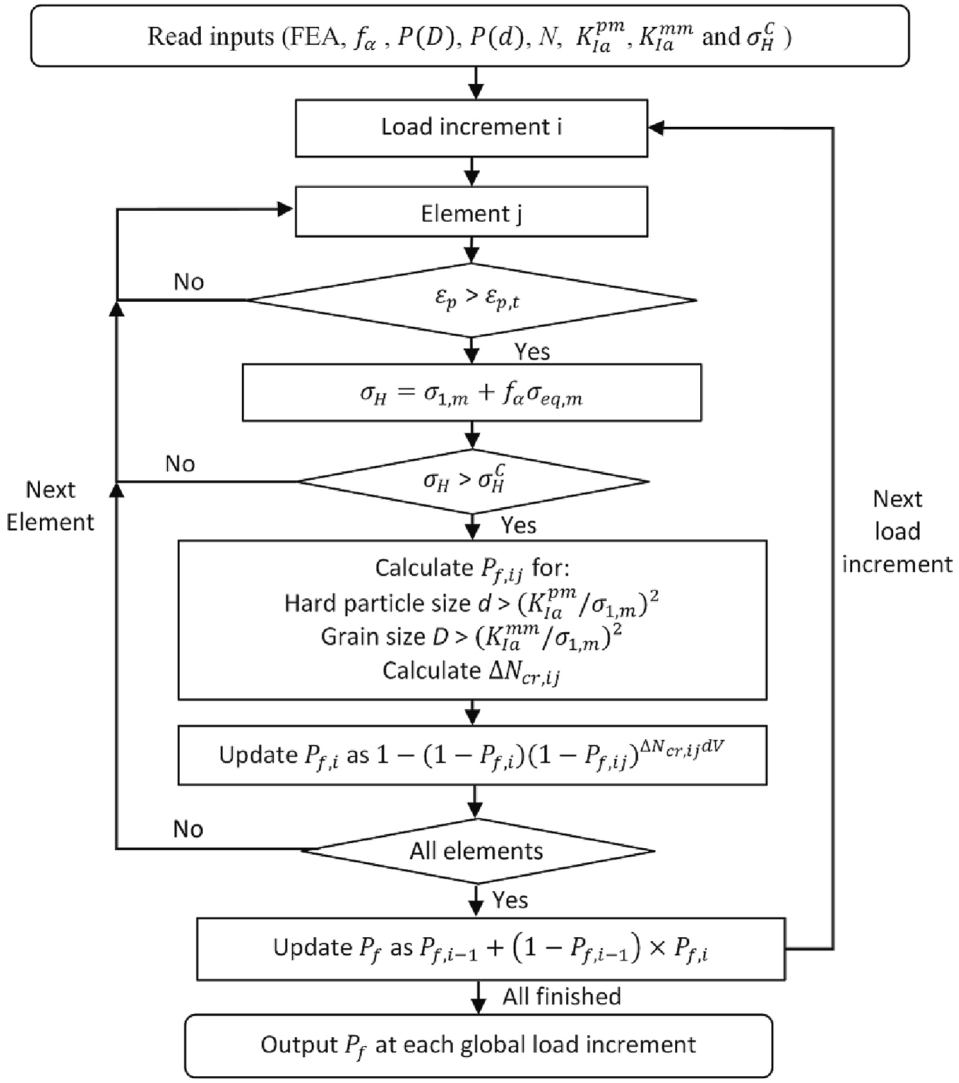

Fig. 5. Flow chart of the computational scheme [29].

Table 4
Values of the general input parameters for all types of steels.

Parameters	Values	Reference
Threshold plasticity strain $\varepsilon_{p,t}$	10^{-5}	[6]
Elementary volume V_0	0.001 mm^3	[6]
Stress factor of inclusion f_α	1.495 for cementite, 0.239 for other inclusions	[36]
Scatter of the inclusion fracture strength $\Delta\sigma_H^C$	0.10 GPa	[29]

and toughness is measured as critical crack tip opening displacement (CTOD) [30–32]. The geometry of the specimen is shown in Fig. 6 and specified in Table 5 for each type of steel, together with the corresponding test temperatures.

SENB specimens are modelled in Abaqus 2017. For each analysis, a quarter of the specimen is modelled as a 3D deformable solid by using symmetry. The support and load roller are modelled as analytical rigid surfaces. The contact between rollers and the specimen is frictionless. Fig. 7 (a) mirrors the quarter of the specimen to show the 3D model of the pre-fatigued specimen and two rollers. Fig. 7 (b) shows the mesh near the crack tip for pre-fatigued specimens. The initial pre-fatigued crack is modelled as a finite notch that is 0.005 mm in tip radius. The smallest element near the crack tip has the dimension 0.001 mm × 0.005 mm × 0.067 mm. Fig. 7 (c) and Fig. 7 (d) show the 3D model and mesh near the crack tip for un-fatigued specimens of ferritic steel. A 20-noded hexahedral element with reduced integration (C3D20R) is used for the mesh. Displacement control is used to apply a total deflection of 1 mm. A full Newton-Raphson algorithm is used to solve the geometric and material nonlinearity in an implicit method.

4. Results

4.1. Determination of cleavage parameters

Cleavage parameters K_{Ia}^{mm} (grain-boundary property) and σ_H^C (brittle-inclusion property) are determined by inverse analysis (maximum likelihood fitting) from the measured CTOD. The cleavage property of particle/interface, which is represented by K_{Ia}^{pm}, is provided by literature [31,32] for martensitic steel and ferritic steel, respectively, and calculated from fracture surfaces analysis at the crack initiation sites for S690 steels.

Examination of fracture surfaces of S690-A1 was performed in our previous study using SEM to characterize the mode of failure and to locate and identify microstructural features that can triggered cleavage [42]. The smallest inclusions that are identified as local cleavage fracture initiation sites are of sizes 1.22 (±0.08) μm and 1.27 (±0.10) μm. The micro-cracks of such inclusion size are able to propagate across the inclusion/matrix interface and form cleavage facets among neighbouring grains. FEA shows that $\sigma_{1,m}$ is in the range of 2000 – 2500 MPa at the location of crack initiation sites. K_{Ia}^{pm} can be determined by eq. (5) with the identified particle size and stress state at the crack initiation site. The same analysis is performed for S690-A2 and S690-B. The value of K_{Ia}^{pm} is calculated as 2.5 MPa$\sqrt{\text{m}}$ (with a standard deviation of 0.2 MPa$\sqrt{\text{m}}$) for S690 steels. For each type of S690 steel, the maximum likelihood fitting is performed on the data including deep cracked ($a/W = 0.5$) and shallow cracked ($a/W = 0.1$ or 0.25) pre-fatigued specimens taken from the top quarter section and the middle section. K_{Ia}^{mm} is separately fitted for top section and middle section, while σ_H^C of square inclusions and circular inclusions is fitted from the combined data of top and middle sections.

The surface energy for microcrack penetration across particle/matrix interface, γ_{pm}, is provided as 17 J/m^2 in [28] for the martensitic steel. Cleavage parameter K_{Ia}^{pm} are calculated by substituting the equation used in [28 & 31]:

$$\sigma_{fracture} = \sqrt{\frac{\pi E \gamma_{pm}}{(1-\nu^2)d_c}} \tag{7}$$

where E is Young's modulus and ν is Poisson's ratio, into $\sigma_{1,m}$ in eq. (5), and the resulting value is 3.5 MPa$\sqrt{\text{m}}$. Cleavage parameters K_{Ia}^{mm} and σ_H^C are fitted from combined CTOD data of three temperatures −60 °C, −40 °C and −20 °C. The material's toughness K_{Jc}(1 T)

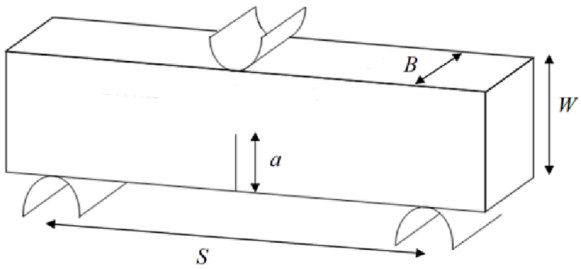

Fig. 6. Geometry layout of the SENB specimen.

Table 5
Geometric information of specimens and test temperatures.

Constraints	Geometry*	Crack length	Materials	Temperatures
$a/W \geq 0.5$	1	10 mm	S690-A1, Top, Middle	−100 °C
			S690-A2, Top, Middle	
			S690-B, Top, Middle	−130 °C
	1		Martensitic	−20, −40, −60 °C
	2			
$a/W = 0.25$	1	5 mm	S690-A1, Top	−100 °C
			S690-A2, Top, Middle	−100 °C
			S690-B, Top, Middle	−130 °C
$a/W = 0.1$	1	2 mm	S690-A1, Middle	−100 °C
Unfatigued	3	7 mm	Ferritic	−110 °C

*Geometry 1: $S = 80$ mm, $W = 20$ mm, $B = 10$ mm; Geometry 2: $S = 72$ mm, $W = 18$ mm, $B = 9$ mm.
Geometry 3: $S = 60$ mm, $W = 20$ mm, $B = 20$ mm.

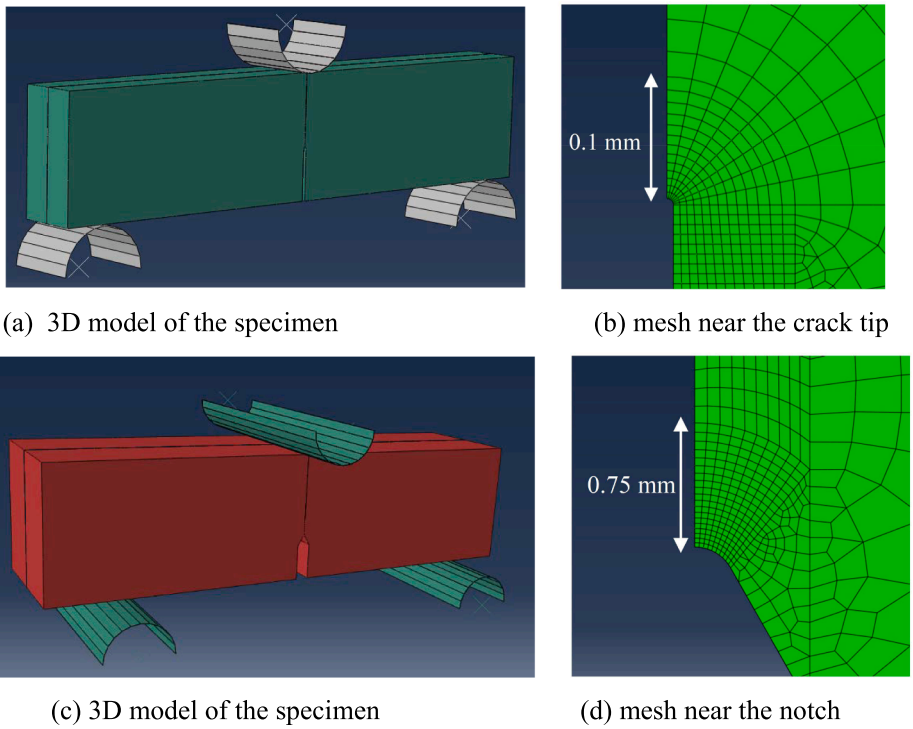

Fig. 7. Finite element model of the (a-b) prefatigued and (c-d) unfatigued three-point bending test.

is<100 MPa$\sqrt{\text{m}}$ at all three temperatures.

For the ferritic steel, fracture tests were conducted using un-fatigued SENB specimens with a notch of 0.25 mm root radius. The CTOD is calculated according to [32] as

$$\text{CTOD} = \frac{K^2(1-\nu^2)}{2\sigma_y E} + \frac{r_p(W-a)V_p}{(r_p(W-a)+a)} \tag{8}$$

where r_p is the rotation factor (=0.4), W is specimen width, a is notch depth, V_p is a plastic component of the notch mouth opening displacement, which is measured by a clip-gauge, and K is the stress intensity factor calculated according to [35]. In [32], the surface energy for microcrack penetration across particle/matrix interface, γ_{pm}, is provided as 10 J/m^2. Cleavage parameter K_{Ia}^{pm} is calculated by substituting the equation

$$\sigma_{fracture} = \sqrt{\frac{4E\gamma_{pm}}{\pi(1-\nu^2)d_c}} \tag{9}$$

used in [32] into $\sigma_{1,m}$ in eq. (5), and the resulting value is 1.7 MPa$\sqrt{\text{m}}$. Cleavage parameters K_{Ia}^{mm} and σ_H^C are fitted from the CTOD values measured at −110 °C. Two out of nine specimens that failed with the ductile mode have been excluded from the present data

points during fitting.

4.2. Summary of calculated cleavage parameters

A summary of the fitted values for cleavage parameters K_{Ia}^{mm} and σ_H^C is presented in Table 6. Fig. 8 shows the experiments and the simulations using the fitted parameters.

Sensitivity studies were performed in [29] for S690-A1. It was found that σ_H^C, K_{Ia}^{pm} and K_{Ia}^{mm} are controlling parameters while $\varepsilon_{p,t}$, V_0, and $\Delta\sigma_H^C$ have little impact with their predefined values in Table 4. Note that σ_H^C is the threshold stress for particle cracking, and with a scatter value $\Delta\sigma_H^C = 0.1$ GPa it also defines the maximum stress for particle cracking. For the bainitic and martensitic steels, the pre-fatigued specimen generates high local tensile stress (greater than2000 MPa) at low CTOD level (<0.01 mm), and during the fitting of σ_H^C and K_{Ia}^{mm} the gradient of simulated CTOD to σ_H^C becomes flat near its optimized value. An uncertainty of 7–10% in the fitted value of σ_H^C exists when one specimen geometry is used. To improve the accuracy of fitting, either two different a/W ratios or multiple temperatures are used to form the dataset of bainitic and martensitic steels. On the contrary, the unfatigued specimen of ferritic steel generates a local tensile stress that is gradually increased, and the gradient of simulated CTOD to σ_H^C remains sharp near its optimized value. The uncertainty of the fitted value of σ_H^C is within 2% when one geometry is used, and the dataset used in Fig. 8 (h) is sufficient to determine cleavage parameters for the studied ferritic steel.

The values of K_{Ia}^{mm} of the S690 steels are in the range of 19.0 to 21.7 MPa$\sqrt{\text{m}}$; the variation is within 15%. σ_H^C of circular inclusions of S690 steels are within 10% variation, ranging in 2.7–2.9 GPa. The cleavage parameter K_{Ia}^{mm} shows slight variation through the thickness of the plate. For S690-A1 and S690-A2, K_{Ia}^{mm} is larger for the top section than for the middle section, while for S690-B, K_{Ia}^{mm} is larger for the middle section than for the top section. σ_H^C value of square inclusions is 10% lower than of circular inclusions in the S690-A1 and S690-A2.

Comparing the S690 steels with the other two types of steel from literature, the martensitic steel shows a value of K_{Ia}^{mm} within 15% difference compared to S690 steels, while the ferrite-cementite steel shows a 30% lower K_{Ia}^{mm}. σ_H^C appears to vary largely. The circular inclusions in the martensitic steel show the largest value, 4.0 GPa, 50% higher than the value in the S690 steels.σ_H^C of cementite shows the lowest value 2.0 GPa, 10% lower than the value of square inclusions in the S690 steels.

5. Discussion

Lower σ_H^C of square inclusions of S690-A1 and S690-A2 are found compared to σ_H^C of circular inclusions, although they are of approximately the same magnitude. This indicates that brittle square inclusions are prone to cracking in both Nb-rich S690-A1 and Ti-rich S690-A2.σ_H^C of cementite shows the lowest value, even if the stress concentration due to larger aspect ratio is considered by the factor f_α. It may be due to the fact that the cementite particles are distributed with a high density and high local stresses may be generated locally in the region of particle clusters as demonstrated by [43], while the model assumes that there is no interaction among particles. The circular inclusions in the low-carbon martensitic steel show a 50% higher σ_H^C value than in the S690 steels. The higher stress threshold of particle cracking could be related to the more complex inclusions in the martensitic steel, which are prone to debonding from the matrix and would not have a tensile stress as high as calculated. However, this significantly higher threshold may also be due to the temperature dependence of cleavage parameters, as the values of martensitic steel are fitted from fracture test at −60 °C to −20 °C, while the fitting of the other steels are at temperature not higher than −100 °C.

The cause of the variation in K_{Ia}^{mm} is possibly be related to sub-grain boundaries, such as packet and block boundaries. The model uses the size of PAG to represent the crack resistance of boundaries, while in S690 steels and the martensitic steel packets and blocks are present within PAGs. Fig. 9 shows the distribution of boundary misorientation angles for the top and middle section of the S690 steels, determined by EBSD. The S690 steels have narrowly varying K_{Ia}^{mm}, which can be explained by the narrow range of the misorientation angle of grain boundaries. There is a slight difference in the fraction of boundaries with 50-60° misorientation angle. The 50-60° misorientation angle corresponds to block boundaries and packet boundaries [30]. Increased fraction of high misorientation angle boundaries is associated with increased K_{Ia}^{mm} values. The low value of K_{Ia}^{mm} of the ferritic steel can similarly be explained by the lack of hierarchical grain structures. The ferrite grains are defined as grains with misorientation angle of 5° or more, and no packets or blocks are observed within the ferrite grains.

The variation in K_{Ia}^{mm} leads to a discussion on whether the PAG or the grain defined by a misorientation angle should be used for modelling cleavage in bainitic and martensitic steels. Fig. 10 [42] shows a transverse section of the fracture path profile in S690-A1 and

Table 6
Summary of cleavage parameters determined for all materials (- stands for not detected).

Materials	K_{Ia}^{mm}(MPa$\sqrt{\text{m}}$)		σ_H^C(GPa) with $\Delta\sigma_H^C = 0.1$ GPa		
	top	middle	Circular inclusions	Square inclusions	Elongated Cementite
S690 –A1	19.7	19.5	2.7	2.2	–
S690 – A2	19.3	19.0	2.7	2.4	–
S690 - B	21.3	22.8	2.9	–	–
Martensitic steel	19.5		4.1	2.4	–
Ferritic steel	14.2		–	–	2.0

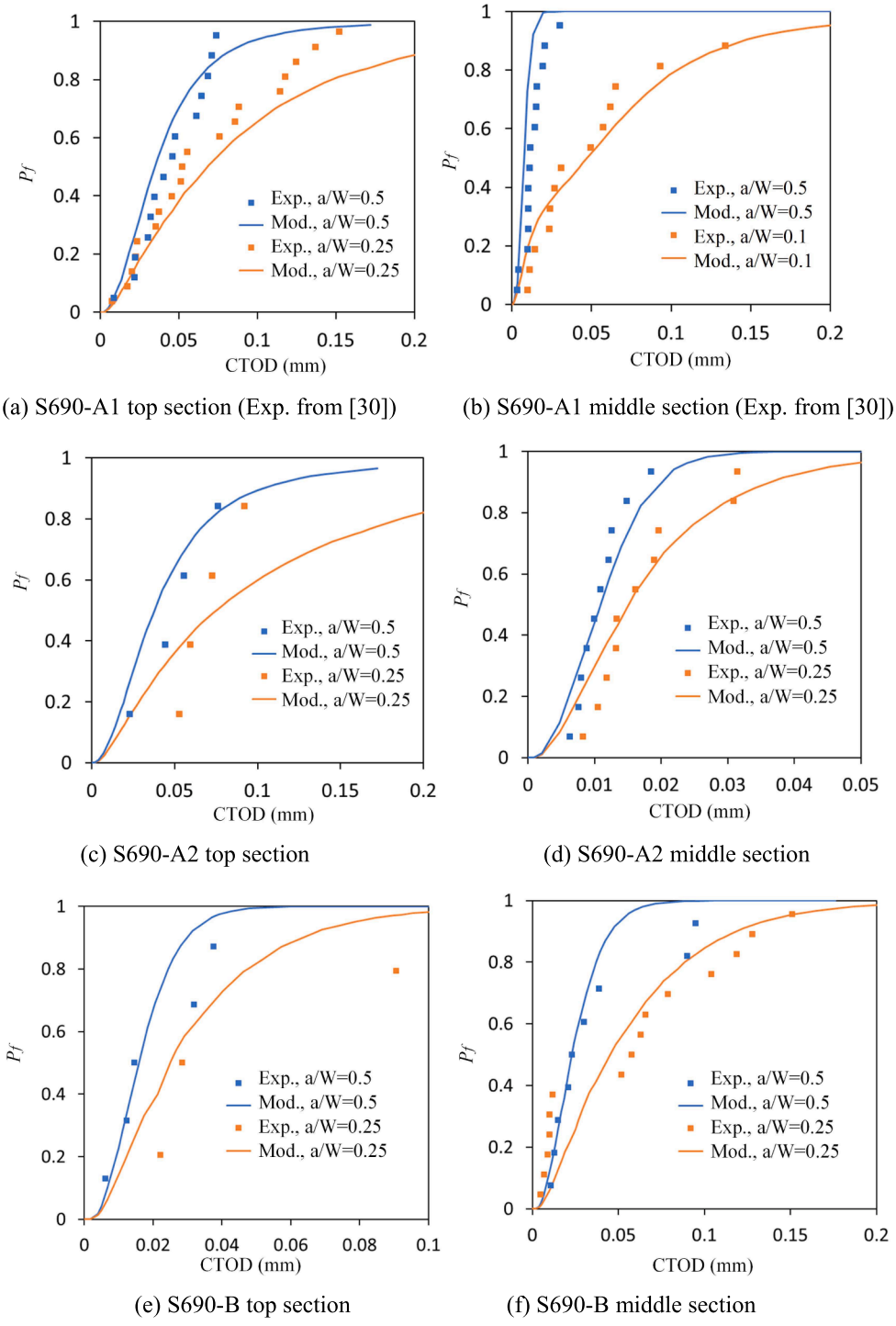

Fig. 8. Cleavage probability calculation based on fitted parameters (Exp. is experimental data and Mod. is modelled distribution).

indicates that not all high misorientation boundaries show the ability to arrest cracks. For almost the entire analysed length (around 95%) of the fracture surface reported in [42], the cleavage crack propagates through the {1 0 0} and {1 1 0} planes in the top and middle sections, where both families of planes have a similar contribution. In both top and middle thickness positions, the crack deflects significantly from its path, or involve plastic deformation (revealed by a poor indexation in EBSD maps), where the neighbouring sub-structure divided by the PAG, packets, or block boundaries has a different Bain axis (for example, the locations indicated

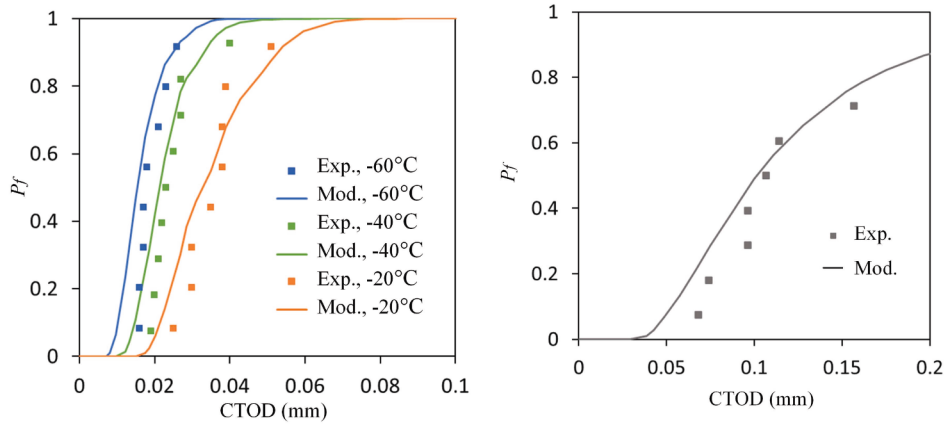

(j) martensitic steel (Exp. from [31]) (h) ferritic steel (Exp. from [32])

Fig. 8. (*continued*).

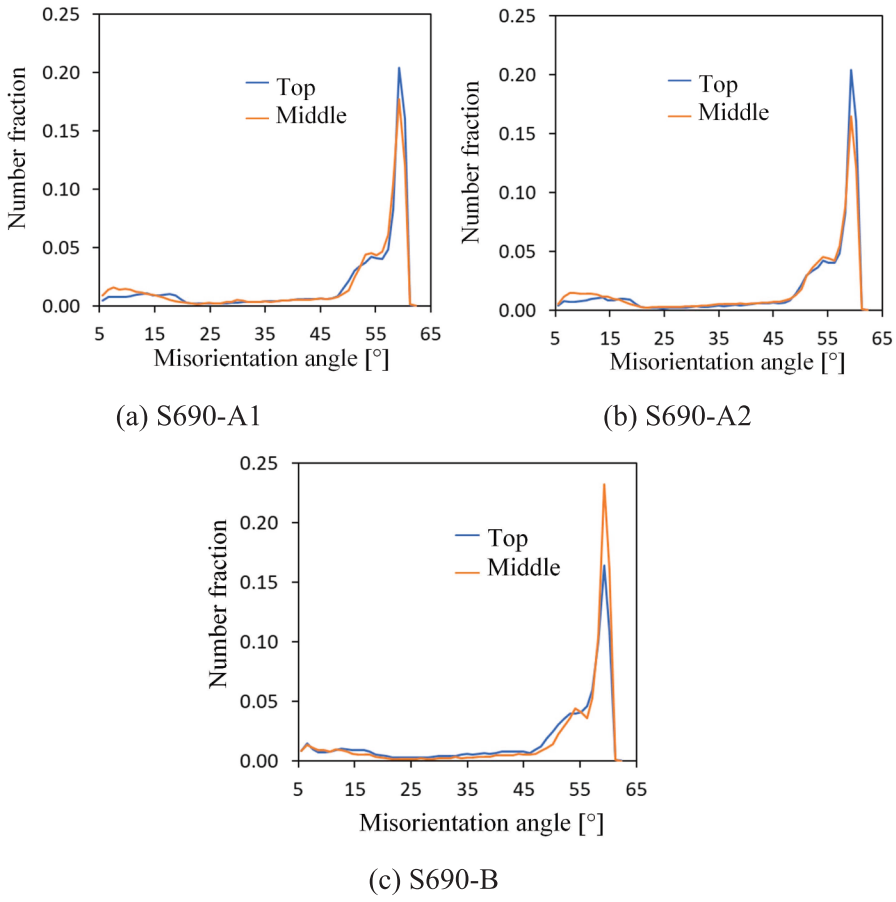

(a) S690-A1 (b) S690-A2

(c) S690-B

Fig. 9. Number fraction of boundary misorientation angles for S690 steels.

by black arrows in Fig. 10 b). According to this finding, the Bain zone is the effective crystallographic microstructural characteristic in deflecting the cleavage crack, which agrees with what was found by Wang et al. [44].

However, boundaries with different Bain axes that do not lead to deflections are also observed, as indicated by blue arrows in Fig. 10 (b). This can be attributed to the thickness of the Bain area, as observed by Wang et al. [44]. The observation in fracture path

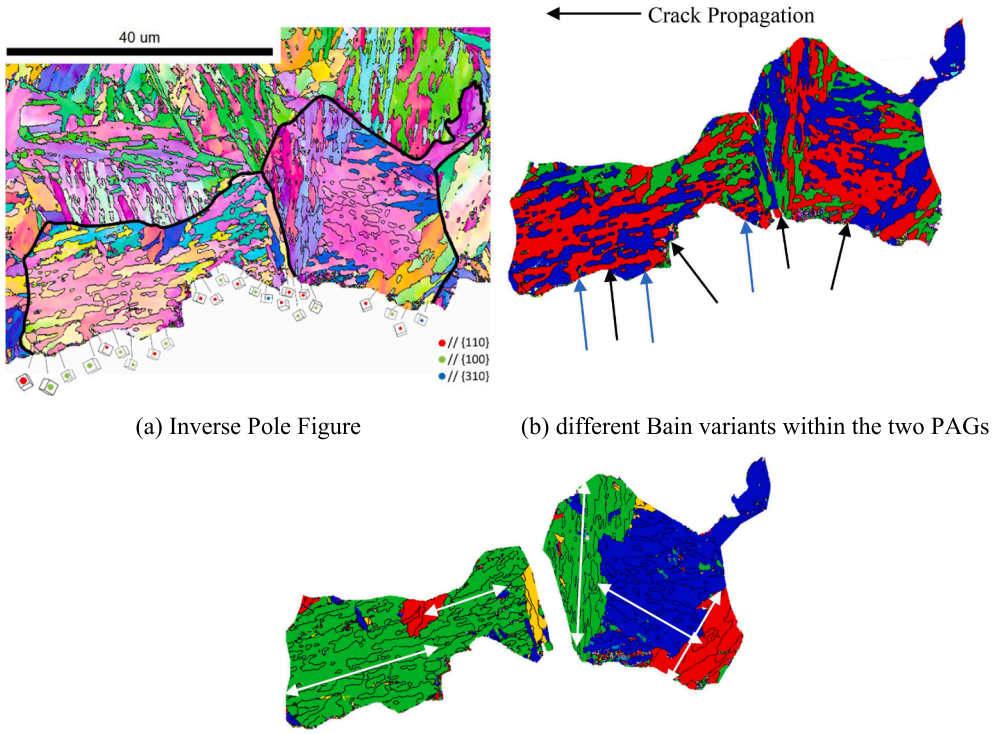

(a) Inverse Pole Figure (b) different Bain variants within the two PAGs

(c) different K-S variants within the two PAGs

Fig. 10. Transverse fracture path profile in S690-A1 measured by EBSD [42] (Thin black lines are high-angle greater than 15° grain boundaries and the thick black contour is the PAG boundary).

profile leads to a difficult determination of the effective size of the Bain area. Fig. 10 (c) shows the K-S variants of the same grains in (a) and (b), with white arrows indicating the approximate length of the large Bain area that can act as an initiation facet if cleavage occurs at the shown plane. Under the assumption that the PAG size is linearly correlated to the K-S packet size and to the possible cleavage facet size, the PAG size represents the microstructural unit, and the corresponding K_{Ia}^{mm} represents the crack resistance of all boundaries within a PAG.

Defining the Bain unit on the basis of the misorientation angle results in a large portion of ultra-small areas that do not act as cleavage facets, which will underestimate the value of K_{Ia}^{mm}. Fig. 11 shows the comparison of the size distribution of PAGs and of bainite grains defined by a misorientation angle of 15° or higher, for the same EBSD scan in the middle section of S690-A2. More than 50% of grains defined by a misorientation angle of 15° have major axis length lower than 2 μm. The 15° definition of grain boundary leads to a fitted $K_{Ia}^{mm} = 11.3\text{MPa}\sqrt{\text{m}}$, which is even 20% lower than the fitted value of the ferritic steel (where ferrite grains are defined by a misorientation angle of 5°).

Among the methods of cleavage modelling proposed in literature, Beremin parameters (σ_u and m) [7] and surface energy parameters (γ_{pm} and γ_{mm}) [20] are most frequently used to represent material's fracture property at continuum-level and micro-level, respectively. Beremin parameters reflect the total effect of geometry of microstructures (e.g., microcrack size distribution, microcrack density) and toughness of microstructures (e.g., resistance of boundaries, cracking criterion of particles). Any changes in the microstructure will affect the Beremin parameters. Fig. 12 shows the normalized (divided by the mean) cleavage parameters (K_{Ia}^{mm} and σ_H^C) presented in Table 6 and Beremin parameters (σ_u and m) determined for the same S690 steels by the method proposed in [45]. (Martensitic steel and ferritic steel are not used for determining Beremin parameters as the method requires a combined dataset of small-scale-yielding and large-scale-yielding.) The material parameters σ_u and m determined by the Beremin method vary in a range of 50% − 230% around the mean. Similar findings of the wide variation of Beremin parameters are reported in [12–14]. In comparison, the current method uses geometric information of microstructures as input, and the determined parameters solely represent effective resistance to fracture for the defined microstructures. Theoretically, the cleavage parameters will not be influenced when grain size or particle size are changed, as long as the phases are the same. Fig. 12 shows that the values of K_{Ia}^{mm} and σ_H^C determined in this paper vary in a range of 95% − 115% around the mean for the S690 steels. The values are highly consistent even for the steels from different sources and different sections of the steel plates.

The surface energy calculated from experimentally measured fractured facet sizes is a more local parameter compared to K_{Ia}^{mm}. The surface energy parameter is used to investigate the boundary of the actual initiation facet, while K_{Ia}^{mm} reflects the statistical equivalent effect of the defined grains. Very few measurements have been reported for bainitic and martensitic steels as their cleavage facets show

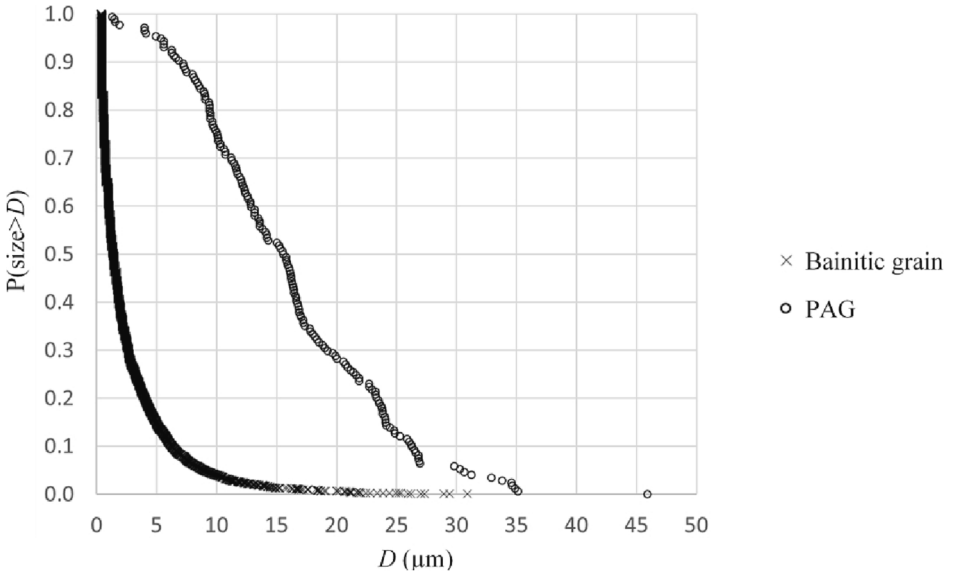

Fig. 11. Size distribution of PAG and of bainite grain defined by 15° misorientation for the microstructure of S690-A2.

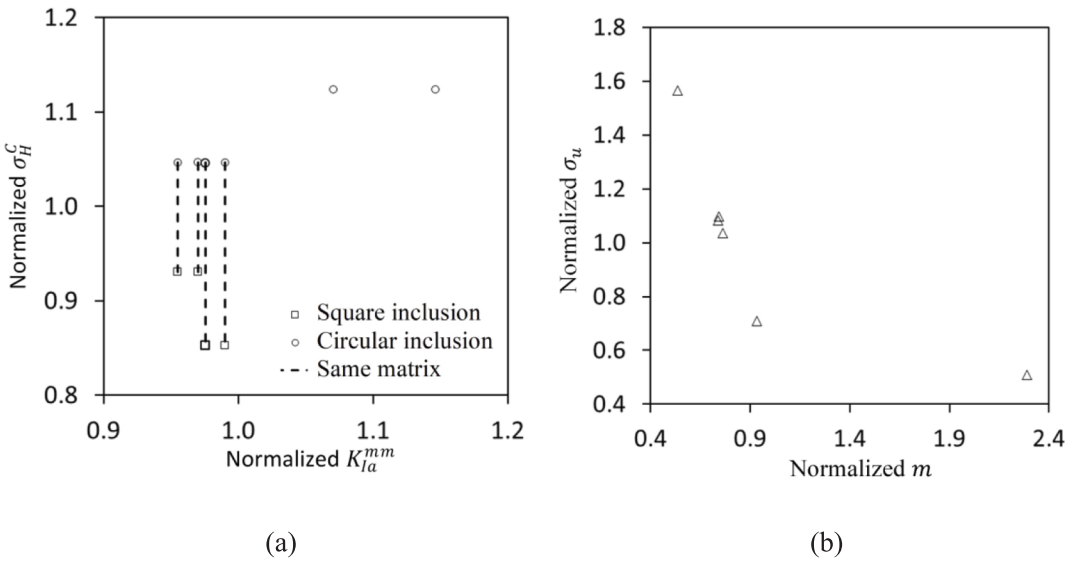

Fig. 12. Cleavage parameters in middle and top sections of S690-A1, A2, B steels calculated by (a) microstructural-informed model herein and (b) Beremin method proposed in [45].

complex morphology. Linaza [25] estimated a γ_{mm} range of 50–200 J/m^2 for martensitic steel at 77 K. For ferritic steels, San Martin and Rodriguez-Ibabe [26] calculated a γ_{mm} range of 110–176 J/m^2 at 77 K. Kawata et al. measured a γ_{mm} range of 25–100 J/m^2 for Ni-ferritic steels at −100 °C [27], considering correction of facet shape and 3D orientation. The values of γ_{mm} reported in literature shows vary in a range of 40% − 160% around the mean for a single type of steel. In comparison, K_{Ia}^{mm} determined in the present study varies in a range of 95% − 115% around the mean for three types of S690 steels. The reason is that surface energy is a parameter measured from each cleavage facet and can vary locally among microstructures. K_{Ia}^{mm} is an effective equivalent to model the macroscopic fracture that has averaged the local variations. When modelling the macroscopic fracture, the cleavage parameters in the present method are more consistent.

6. Conclusions

In the current paper, a statistical modelling approach is applied to estimate the cleavage parameters across different types of steels.

Cleavage parameters are compared among three tempered bainitic (S690) steels, an as-quenched martensitic steel, and a ferritic steel. The top quarter and middle sections of the S690 steels are separately modelled in terms of tensile properties, grain sizes, inclusion distribution, and cleavage parameters. The other two types of steels are studied for a single thickness position. The tensile properties, grain sizes, and inclusion distributions of the latter two types of steel are taken from literature. The following conclusions are highlighted:

- The values of cleavage parameter K_{Ia}^{mm} are within 15% variation among all three S690 steels considered in this study, including two different sources. The values of cleavage parameter σ_H^C are within 10% variation for the same type of inclusions.
- The cleavage parameters K_{Ia}^{mm} for S690 steels are more similar to the martensitic steel than to the ferrite-cementite steel. The values of cleavage parameter σ_H^C vary significantly from 2.0 GPa to 4.1 GPa among the steels.
- The variation of cleavage parameter K_{Ia}^{mm} can be explained by the hierarchical grain structure of steels. The value represents the total effect of high misorientation boundaries of a grain on crack arrest.
- The cleavage parameters determined in this paper show high degree of consistency across different types of steels, which allows the usage of the calculated values in microstructure designs to control macroscopic toughness.

The current method has the following limitations that could be investigated further:

- The current model does not account for the temperature dependence of cleavage parameters.
- Dynamic fracture behaviour is not investigated in this paper.

CRediT authorship contribution statement

Quanxin Jiang: Visualization, Validation, Methodology, Investigation, Formal analysis, Data curation, Conceptualization, Writing - original draft, Writing - review & editing. **Virgínia M. Bertolo:** Writing – review & editing, Validation, Methodology, Investigation, Data curation, Conceptualization. **Sakari Pallaspuro:** Writing – review & editing, Investigation, Data curation, Conceptualization. **Vera Popovich:** Writing – review & editing, Validation, Supervision, Methodology, Conceptualization. **Jilt Sietsma:** Writing – review & editing, Supervision, Methodology, Conceptualization. **Carey L. Walters:** Writing – review & editing, Supervision, Methodology, Conceptualization.

Declaration of Competing Interest

The authors declare that they have no known competing financial interests or personal relationships that could have appeared to influence the work reported in this paper.

Data availability

Data will be made available on request.

Acknowledgement

The authors acknowledge the support in the Micro-Tough research project (n. 16350) from the Dutch Research Council (NWO) and the consortium of partners that include Allseas Engineering, Dillinger, Lloyd's Register, The Dutch Ministry of Defence, and TNO.

References

[1] Miyata T, Yang RC, Otsuka A, Haze T, Ahira S. Cleavage fracture of steels with fine grained ferrite, coarse grained bainitic and martensitic. Proceeding of the seventh international conference of fracture 1989:2563–71.
[2] Lee S, Kim S, Hwang B, Lee BS, Lee CG. Effect of carbide distribution on the fracture toughness in the transition temperature region of an SA 508 steel. Acta Mater 2002;50(19):4755–62.
[3] Ray A, Paul SK, Jha S. Effect of inclusions and microstructural characteristics on the mechanical properties and fracture behavior of a high- strength low- alloy steel. J Mater Engng Perform 1995;4(6):679–88.
[4] Li X, Ma X, Subramanian SV, Shang C, Misra RDK. Influence of prior austenite grain size on martensite-austenite constituent and toughness in the heat affected zone of 700MPa high strength linepipe steel. Mater Sci Engng A 2014;616:141–7.
[5] Zhou MW, Yu H. Effects of precipitates and inclusions on the fracture toughness of hot rolling X70 pipeline steel plates. Int J Miner Metall Mater 2012;19(9):805–11.
[6] Pineau A, Benzerga AA, Pardoen T. Failure of metals I: Brittle and ductile fracture. Acta Mater 2016;107:424–83.
[7] Beremin FM. A local criterion for cleavage fracture of a nuclear pressure vessel steel. Metall Trans A 1983;14A:2277–87.
[8] Wallin K, Saario T, Törrönen K. Statistical model for carbide induced brittle fracture in steel. Metal Science 1984;18(1):13–6.
[9] Lin T, Evans AG, Ritchie RO. A Statistical Model of Brittle Fracture by Transgranular Cleavage. Mrch Phys Solids 1986;34(5):477–97.
[10] Martín-Meizoso A, Ocaña-Arizcorreta I, Gil-Sevillano J, Fuentes-Pérez M. Modelling cleavage fracture of bainitic steels. Acta Metall Mater 1994;42(6):2057–68.
[11] Chen JH, Wang GZ, Wang HJ. A Statistical Model for Cleavage Fracture of Low Alloy Steel. Acta Metall 1996;44(10):3979–89.
[12] Bernauer G, Brocks W, Schmitt W. Modifications of the Beremin model for cleavage fracture in the transition region of a ferritic steel. Engng Fract Mech 1999;64:305–25.
[13] Bordet SR, Karstensen AD, Knowles DM, Wiesner C,S.. A new statistical local criterion for cleavage fracture in structural steel. Part I: model presentation. Engng Fract Mech 2005;72:435–52.

[14] Gao X, Zhang G, Srivatsan TS. Prediction of cleavage fracture in ferritic steels: A modified Weibull stress model. Mater Sci Engng A 2005;394(1–2):210–9.
[15] Lambert-Perlade A, Gourgues AF, Besson J, Sturel T, Pineau A. Mechanisms and modeling of cleavage fracture in simulated heat-affected zone microstructures of a high-strength low alloy steel. Metall Mater Trans A 2004;35(13):1039–53.
[16] Shibanuma K, Nemoto Y, Hiraide T, Suzuki K, Sadamatsu S, Adachi Y, et al. A strategy to predict the fracture toughness of steels with a banded ferrite–pearlite structure based on the micromechanics of brittle fracture initiation. Acta Mater 2018;144:386–99.
[17] Kunigita M, Aihara S, Kawabata T, Kasuya T, Okazaki Y, Inomoto M. Prediction of Charpy impact toughness of steel weld heat-affected zones by combined micromechanics and stochastic fracture model – Part I: Model presentation. Engng Fract Mech 2020;230:106965.
[18] Irwin G. Fracture dynamics. In: Fracturing of Metals, vol. 8. Cleveland: American Society of Metals; 1948. p. 147–66.
[19] Orowan E. Fracture and strength of solids, in. Voll. XII.185: Reports in Progress in Physics; 1948.
[20] Griffith A. The phenomena of rupture and flow in solids. Philos Trans R Soc Lond A 1921;221:163–98.
[21] Curry DA, Knott JF. Effects of microstructure on cleavage fracture stress in steel. Metal Science 1978;12(11):511–4.
[22] Bowen K, Druce SG, Knott JF. Effects of microstructure on cleavage fracture in pressure vessel steel. Acta metal 1986;34:1121–31.
[23] Alexander DJ, Bernstein IM. Cleavage fracture in pearlitic eutectoid steel. Metal Trans A 1989;20:2321–35.
[24] Linaza MA, Romero JL, Rodríguez-Ibabe JM, Urcola JJ. Cleavage fracture of microalloyed forging steel specimens. Scripta Metall Mater 1995;32:395–400.
[25] Linaza MA, Rodríguez-Ibabe JM, Urcola JJ. Determination of the energetic parameters controlling cleavage fracture initiation in steel specimens. Fatig Fract Eng Mater Struct 1997;20:619–32.
[26] San Martin JI, Rodriguez-Ibabe JM. Determination of energetic parameters controlling cleavage fracture in a Ti-V microalloyed ferrite-pearlite steel. Scripta Mater 1999;40:459–64.
[27] Kawata I, Nakai H, Aihara S. Experimental evaluation of effective surface energy for cleavage microcrack propagation across grain boundary in steels. Acta Mater 2018;150:40–52.
[28] Li Y, Pallaspuro S, Ren X, He J, Kömi J, Zhang Z. A multi-barrier model assisted CAFE method for predicting ductile-to-brittle transition with application to a low-carbon. Mech Mater 2021;153:103669.
[29] Jiang Q, Bertolo VM, Popovich VA, Sietsma J, Walters CL. Microstructure-informed statistical modelling of cleavage fracture in high strength steels considering through-thickness inhomogeneities. Engng Fract Mech 2022;267:108432.
[30] Bertolo VM, Jiang Q, Scholl S, Petrov R, Hangen U, Walters CL, et al. A comprehensive characterisation and quantification of the multiphase microstructure of a thick-section high strength steel. J Mater Sci 2022;57:7101–26.
[31] Pallaspuro S, Mehtonen S, Kömi J, Zhang Z, Porter D. Effects of local grain size and inclusions on the low-temperature toughness of low-carbon as-quenched martensite. Mater Sci Engng A 2019;743:611–22.
[32] Shibanuma K, Aihara S, Suzuki K. Prediction model on cleavage fracture initiation in steels having ferrite-cementite microstructures - Part II: Model validation and discussions. Eng Fract Mech 2016;151:181–202.
[33] Morris JW, Kinney C, Pytlewski K, Adachi Y. Microstructure and 756 cleavage in lath martensitic steels. Sci Technol Adv Mater 2013;14(1):014208.
[34] De Hoff RT. The determination of the size distribution of ellipsoidal particles from measurements made on random plane sections. Trans TMS-AIME 1962;224:474–86.
[35] ISO 2018;12135. Metallic materials - Unifed method of test for the determination of quasistatic fracture toughness.
[36] Jiang Q, Bertolo VM, Popovich VA, Sietsma J, Walters CL. Relating local stress on a hard microstructural inclusion from far-field stress on matrix to understand cleavage fracture in high strength steel. Int J Fract 2021;232:1–21.
[37] Shibanuma K, Aihara S, Ohtsuka S. Observation and quantification of crack nucleation in ferrite-cementite steel. ISIJ Int 2014;54:1719–28.
[38] Shibanuma K, Nemoto Y, Hiraide T, Suzuki K, Aihara S. Investigation of micro-crack initiation as a trigger of cleavage fracture in ferrite-pearlite steels. ISIJ Int 2017;57:365–73.
[39] Nemoto Y, Shibanuma K, Suzuki K, Sadamatsu S, Adachi Y, Aihara S. 3D observation of micro-cracks as cleavage fracture initiation site in ferrite-pearlite steel. ISIJ Int 2017;57:746–54.
[40] Kroon M, Faleskog J. Influence of crack deflection into the carbide/ferrite interface on cleavage fracture initiation in ferritic steels. Mech Mater 2008;40:695–707.
[41] Qiao Y. Modeling of resistance curve of high-angle grain boundary in Fe-3wt% Si alloy. Mater Sci Eng A 2003;361:350–7.
[42] Bertolo VM, Jiang Q, Tiringer U, Walters CL, Sietsma J, Popovich VA. Cleavage fracture micromechanisms in thick-section high strength steels. J Mater Sci 2022;57:20033–55.
[43] Wang Z, Chen T-K, Lloyd DJ. Stress distribution in particulate-reinforced metal-matrix composites subjected to external load. Metall Trans A 1993;24(1):197–207.
[44] Wang X, Wang Z, Xie Z, Ma X, Subramanian S, Shang C, et al. Combined effect of M/A constituent and grain boundary on the impact toughness of CGHAZ and ICCGHAZ of E550 grade offshore engineering steel. Math Biosci Eng 2019;16:7494–509.
[45] Gao X, Ruggieri C, Dodds RH. Calibration of Weibull stress parameters using fracture toughness data. Int J Fract 1998;92(2):175–200.